**SIRM 2015 – 11th International Conference on Vibrations in Rotating Machines,
Magdeburg, Deutschland, 23. – 25. Februar 2015**

# A numerical performance analysis of a gas foil bearing including structural modifications by applying metal shims

**Robert Hoffmann**[1] **Tomasz Pronobis**[1] **Robert Liebich**[1]

[1] Fachgebiet Konstruktion und Produktzuverlässigkeit, TU Berlin, Deutschland, robert.hoffmann@tu-berlin.de

**Abstract**

Gas foil bearings (GFBs) feature numerous advantages, e.g. a low power loss, a high speed operation and the omission of an oil system, it may provide an appropriate bearing setup for small and medium-sized turbo machineries. Nevertheless, sub synchronous vibrations can significantly affect the rotor dynamic behaviour, as shown in experimental and numerical investigations. In general, these vibrations are caused due to two reason: The non-linear fluid film forces and the elastic structure. Particularly, the structure is tunable and has a main influence on the damping and stiffness characteristic of a GFB. Due to friction the elastic structure, damping is supplied and can decrease amplitudes up to a certain level. However, several structural modifications have been introduced to improve static and dynamic performance. One of the most inexpensive modifications is the usage of metal shims, which are inserted between the bump-foil and the bearing sleeve. A defined pre-load is generated inside the elastic structure, which improves the structural behaviour and increases the onset speed of sub synchronous vibrations (OSSV).
The aim of this paper is to examine the effect of a shimmed bearing configuration on the static and dynamic performance. Dynamic linearised bearing parameters "stiffness" and "damping" are calculated by a perturbation method. Both are used for a linearised eigenvalue problem, which is an appropriate method to evaluate the OSSV generated by the self-excitation due to the fluid film. The Reynolds equation is discretised by a hybrid finite difference scheme, while the pressure field is coupled with a 2d plate model. The bump structure is simplified by a link-spring model, which is comparable to the work of Feng et al. [1]. This model includes Coulomb friction effects inside the elastic corrugated structure and captures the interaction between the single bumps. The effect of shimming on the nominal bearing clearance is analysed by using a 2d non-linear FEA. The results show that, due to increased direct stiffness and increased orthotropic effects, the shimmed GFB may increase the OSSV up to 357% for the 5N loading case. In addition, the static magnitude of the eccentricities is reduced for the shimmed GFB, thus smaller film thickness and lower drag torques are present.

## 1 Introduction

Gas foil bearings (GFBs) have a lot of advantages, e.g. a low power loss, high speed operation, high temperature endurability and the omission of an oil system, which may provide an appropriate bearing setup for small and medium-size turbo machinery applications, ref. [2]. In general, GFBs are based on an aerodynamic pressure, which is induced by a generated flow between the turning journal and the top foil (see figure 1 (a)). The main difference between a gas bearing with a rigid housing and a GFB is the elastic bearing structure. It comprises one or more thin metal foils supported by an underlying structure, e.g. corrugated bump foils or metal mesh structures. The dynamic pressure deforms the elastic structure and an optimal film thickness is achieved due to a self-acting behaviour. Thus, a higher load capacity compared to rigid gas bearings is possible, ref. [3] and structural damping is induced by friction contacts inside the compliant structure. The structural behaviour is highly non-linear and is influenced by the excitation frequency, the amplitude of excitation and the static pre-load of the structure, ref. [4, 5, 6]. However, experimental and numerical investigations of GFBs have shown non-linear vibrations, where sub synchronous vibrations, (ref. [3, 7, 8, 9, 10]) and super synchronous vibrations (ref. [7, 11, 8, 10, 9]) are present. Especially, the sub synchronous amplitudes can significantly affect the rotor dynamic performance. If a sub synchronous whirl frequency corresponds with a critical speed of the mechanical system, the sub synchronous amplitudes will result in high displacements (ref. [3, 7, 8, 9, 10]). The rotor speed at the sudden rise of sub synchronous vibrations is called *Onset Speed of Sub synchronous Vibration* (OSSV). The cause of these non-linear vibrations is based on the self-excitation due to non-linear fluid film forces (ref. [12]) and the forced non-linearity due to the elastic structure

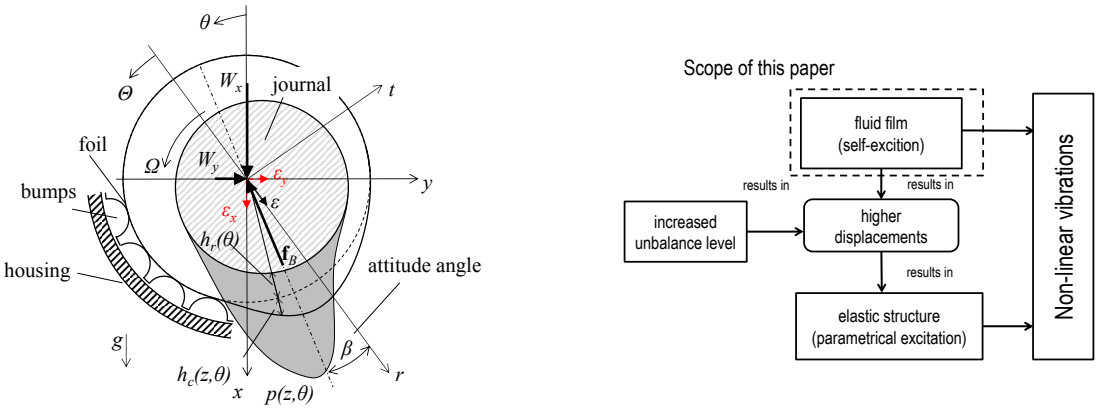


(a) (b)

**Figure 1**: (a) Schematic GFB with a dynamic pressure field $p(\theta, z)$ (b) flow chart non-linear vibrations GFB

(ref. [13]). Considering a perfectly balanced system which is isolated from any kind of surrounding excitations, the only cause of non-linear vibrations can be a self-excitation. It results in higher rotor displacements, which generates a forced non-linearity due to the elastic structure. If damping is sufficient this may lead to a high amplitude stable limit cycle, ref. [9, 14, 3]. Note this effect can be amplified by higher unbalances [15, 11, 9] (see figure 1 (b)). However, for evaluating the OSSV ref. [12] has shown, that a linearised system has a good and conservative correlation between the onset speed of instability (OSI) and the onset speed of sub harmonic vibration (OSSV). The results have shown a typical non-linear vibration, where the sub harmonic amplitudes dominate the vibration characteristics.

Nevertheless, higher rotor displacements need to be restricted to improve the efficiency and lifetime of the overall machinery. Therefore, several passive methods and devices have been introduced to avoid these non-linear vibrations in order to increase the static and dynamic performance. The improvement of the fluid film damping and stiffness characteristic results in an increased performance. Direct modifications by axial [16, 17] or radial pressurizations [18, 19] increase the OSSV. Enhancing damping and stiffness characteristics of the elastic structure also results in an improved dynamic behaviour. Applying a copper coating between the top and the bump foil contact areas the frictional behaviour will be improved and yields higher damping and stiffness values (ref. [20]), thus higher load capacities are possible, ref. [15]. Using a thin layer of a viscoelastic material between top- and bump-foil may generate larger values of stiffness and damping, ref. [21]. Structural modifications, e.g. variable stiffness distributions along the axial or/and the circumferential direction, influence the fluid film and can improve the dynamic performance, ref. [22], splitting of bumps can modify the stiffness in axial direction. The fixed bump leads to higher stiffness due to lower displacements compared to the free bump, ref. [15, 3, 23]. Inserting metal shims between the bearing sleeve and bump structure generates a higher mechanical pre-load, which results in enlarged structural stiffness and damping, ref. [10], while the nominal clearance is affected by shims. This modification has a direct influence on the aerodynamic wedge and can result in higher dynamic pressure, ref. [10][9]. Hence, there is symbiosis of structural and fluid film effects, which needs to be considered when analysing devices in order to achieve higher OSSV. Numerical analyses confirm the positive benefit of a shimmed GFB, ref. [9][10][12]. However, in [9] and [10] the GFB was tested only for low loaded states ($\approx 1-5$N) and the numerical models [9][10][12] do not consider any effects of the complex non-linear structure.

No previous study has investigated the influence of a shimmed GFB in detail while considering a non-linear structural model. In this paper, a static and dynamic analysis of a first generation GFB (Case 1) and a shimmed GFB (Case 2) will be performed. Case 1 will be used for comparison between the shimmed GFB (Case 2) to emphasise the positive effects due to shims. Therefore, three different bearing loads (5, 15 and 30N) will be analysed in static and dynamic performance simulations. The OSSV is evaluated by using the linearised OSI, which is calculated by an eigenvalue problem based on linearised bearing parameters (stiffness and damping). There are three primary aims of this work:

1. Using a non-linear elastic model which considers the frictional contacts and a bump interaction.
2. Analysing the effect of shimming on the nominal bearing clearance by using a non-linear FEA.
3. A numerical investigation of a first generation GFB and a shimmed first generation GFB will be performed for static and dynamic performance.

It is important to note, that the investigation is limited to small perturbations around the equilibrium position.

## 2 Numerical model

Figure 1 (a) shows the compliant structure of a simple GFB. Therein is a turning journal with an angular speed $\Omega$ and its centre is displaced by eccentricities $\varepsilon_x$ and $\varepsilon_y$. Hence, a forced slip stream with a height of $h(z,\theta)$ is induced and results in a dynamic pressure field $p(z,\theta)$. Due to the presence of the pressure field a reacting force $\{\mathbf{f}_B\}$ is generated. For an equilibrium condition the sum of the loading vector $\{\mathbf{w}\} = \{W_x, W_y\}^T$ and the reacting force vector $\{\mathbf{f}_B\}$ must be zero. The reacting force is calculated by integration of the pressure field along the axial and circumferential directions (Eq. (1)). It acts under the attitude angle $\beta = f(\varepsilon, \mathbf{w})$.

$$\{\mathbf{f}_B\} = -R \int_0^l \int_0^{2\pi} (p(z,\theta) - p_a) \begin{Bmatrix} \cos\theta \\ \sin\theta \end{Bmatrix} \mathrm{d}z\mathrm{d}\theta \tag{1}$$

Eq. (2) describes a perfectly aligned journal, expansion effects due to temperature gradients and centrifugal forces are neglected. The film height is composed of two parts: A rigid term $h_r$ influenced by the journal centre displacements including the nominal clearance and by the compliant term $h_c$, respectively. $h_c$ is the deformation of the elastic structure due to an acting pressure field. It is described by a structural model as shown below.

$$h(\theta, z) = \underbrace{c\,(\theta) + \varepsilon_x \cos(\theta) + \varepsilon_y \sin(\theta)}_{h_r(\theta)} + h_c(\theta, z) \tag{2}$$

The pressure field is calculated by solving the normalised Reynolds equation for a compressible, isothermal and isoviscous fluid as given by Eq. (3). It links the pressure field with the film thickness under the presence of a journal rotation $U = R\Omega$. Where $P = p/p_a$, $H = h/c$, $Z = z/R$, $\tau = t\omega_s$, $\Lambda = 6U\mu_a R/\left(p_a c^2\right)$ and $\sigma = 12\omega_s\mu_a R^2/\left(p_a c^2\right)^2$

$$\frac{\partial}{\partial\theta}\left(PH^3\frac{\partial P}{\partial\theta}\right) + \frac{\partial}{\partial Z}\left(PH^3\frac{\partial P}{\partial Z}\right) = \Lambda\frac{\partial}{\partial\theta}(PH) + \sigma\frac{\partial}{\partial\tau}(PH) \tag{3}$$

The boundary conditions are applied: $P(\theta, Z=0) = P(\theta, Z=1) = 1$ and $P(\theta=\theta_1, Z) = P(\theta=\theta_2, Z) = 1$. Note if the pressure falls underneath the ambient pressure condition $P(\theta, Z) < 1$ a top foil lift-off can be present. To avoid negative displacements the sub ambient pressures are set to ambient conditions.

### 2.1 Structural model

A detailed description of the two non-linearities caused by the fluid film and the elastic structure needs to be captured during the calculation process. However, these kind of non-linear elastic structure effects are very time consuming. Hence, a model needs to be introduced, which includes following features and assumptions:

1. The top foil displacements includes axial and circumferential components.
2. Non-linear frictional contacts between top- and bump-foil and bump-foil and housing are taken into account by using the Coulomb model.
3. Each bump $i$ can interact with its surrounding bumps $i-1$ and $i+1$.
4. The applied bump load is concentrated on the top centre of the bump.
5. Bumps are reduced towards rigid segments linked by pivots, while bump interactions are transmitted by linear springs.
6. The bump deformation along the axial direction is assumed to be constant, while longitudinal deformation of the bumps are neglected.
7. No bump-foil separation from the housing is possible.
8. All deformations are elastic.

The top foil is modelled by a thin 2d Timoshenko plate, while 3d effects due to normal tensions are neglected. Hence, a 3d shell can be reduced to a 2d plate model, ref. [24]. The plate finite elements are linked to equivalent non-linear bump spring-damper elements (figure 2 (b)). The global stiffness matrix $[\mathbf{K}^*]$ comprises the bump system matrix $[\mathbf{K}_B^*] = f(p(\theta, z), \mu, \chi)$ and the foil system matrix $[\mathbf{K}_F^*]$. Note the bump matrix is a function of the loading state and the frictional contacts.

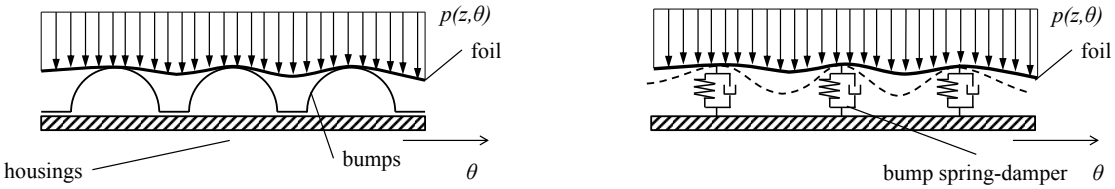


(a) GFB Structure (b) GFB Structure Model

**Figure 2**: GFB Structure: (a) real structure and (b) model (bump spring model and top foil plate model)

$$[\mathbf{K}^*] = [\mathbf{K}_B^*] + [\mathbf{K}_F^*] \tag{4a}$$

$$\{\mathbf{u}_p^*\} = [\mathbf{K}^*]^{-1}\{\mathbf{f}_p\} \tag{4b}$$

An integration of the difference pressure $\Delta p = p(z, \theta) - p_a$ over the top foil surface yields the element force vector $\{\mathbf{f}_p\}$. The displacement of the compliant structure model due to an acting pressure force is given by Eq. (4b). Finally, the compliant film thickness is a subset of the displacement vector $h_c(\theta, z) \subseteq \{\mathbf{u}_p^*\}$. In addition, the top foil Young-modulus $E$ is increased by a factor of 4 to obtain appropriate sagging effects between adjacent bumps, ref. [23].

### 2.2 Non-linear bump spring-damper model

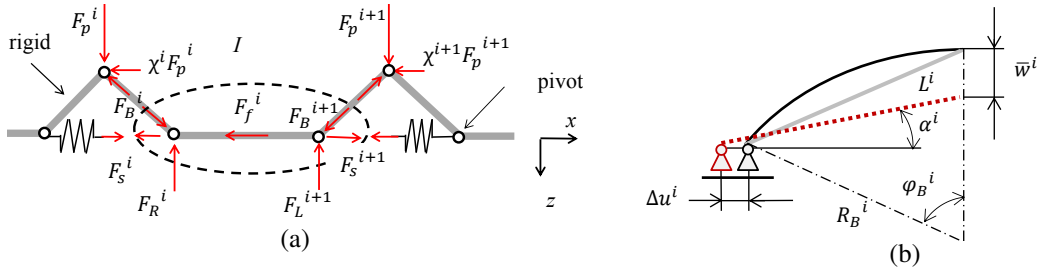


**Figure 3**: Linked spring model: Free punch of a single interacting bump segment $i$ (a) Kinematic of a rigid bump lever (b)

The calculation of the bump stiffness is based on the work of Feng et al [1]. However, this model is extended towards a shimmed application. In addition, due to the numerical challenge of describing the discontinuous Coulomb friction displacement $\Delta u^i$, which significantly affects the interaction forces of a single bump lever, a simple under relaxation procedure is applied: $\left\{\Delta u^i\right\}^n = \zeta_B \left\{\Delta u^i\right\}^n + (1 - \zeta_B) \left\{\Delta u^i\right\}^{n-1}$, with $\zeta_B = 0.6 - 0.9$. At each bump pitch every single axial node is linked in parallel with an equivalent bump spring-damper ($k_B^i$ and $c_B^i$). This assumption is receivable, due to the rigid links and the relationship between horizontal and vertical deflection of all bumps, see figure 3 a). Thus the rigid lever kinematic is reduced to a vertical bump spring-damper. Each bump is simplified to tow rigid pivoted levers, which are connected to a bump segment "$I$". The interaction forces $F_s^i$ and $F_s^{i+1}$ between the rigid bump segment are transduced by single vertically spaced springs $k_s$. It is deformed by the horizontal bump displacements $\Delta u^i$ and $\Delta u^{i+1}$, see figure 3 a). Note $k_s$ (see appendix) depends on the bump material and geometry and is constant for a single bump. It is calculated by using an energetic relationship described

by Castigliano's theorem, ref. [1, 25]. The kinematic relationship between the vertical bump displacement $\Delta\overline{w}^i$, which is based on the arithmetic average of the top foil displacement along the axial direction $z$, and the horizontal displacement $\Delta u^i$ (Eq. (5a)) depends on the angle $\alpha^i$ (Eq. (5b)), see figure 3 (b).

$$\Delta u^i = \sqrt{\left(2R_B \sin\left(\frac{\varphi_B^i}{2}\right)\right)^2 - \left(R_B\left(1-\cos\left(\varphi_B^i\right)\right) + \Delta\overline{w}^i\right)^2} - R_B \sin\left(\varphi_B^i\right) \tag{5a}$$

$$\tan\alpha^i = \frac{R_b\left(1-\cos\left(\varphi_B^i\right)\right) - \Delta\overline{w}^i}{R_B \sin\left(\varphi_B^i\right) + \Delta u^i} \tag{5b}$$

The force equilibrium in the horizontal direction is given by Eq. (6).

$$F_f^i = F_s^{i+1} + F_{B,x}^i - F_s^i - F_{B,x}^{i+1} \equiv F_x^i \tag{6}$$

The bump lever forces $F_B^i = F_R^i / \tan\alpha^i$ and $F_B^{i+1} = F_L^i / \tan\alpha^{i+1}$ as well as the interaction forces $F_s^i = 2\Delta u^i k_s$ and $F_s^{i+1} = 2\Delta u^{i+1} k_s$ are related to the bump kinematic. Note the right and left vertical forces ($F_R^i$ and $F_L^i$) are affected by the concentrated applied bump loading $F_p^i$, which is calculated by the integration of the pressure field, and the friction forces due to the interference of top- and bump-foil. Using the momentum equilibrium gives:

$$F_R^i = \frac{1}{2} F_p^i \cdot \left(1 - \chi^i \tan\alpha^i\right) \tag{7a}$$

$$F_L^i = \frac{1}{2} F_p^i \cdot \left(1 + \chi^i \tan\alpha^i\right) \tag{7b}$$

Where the friction force between the bump segment $i$ and the housing is generated by the normal forces $F_R^i$ and $F_L^i$.

$$F_f^i = \mu^i \cdot \left(F_R^i + F_L^{i+1}\right) \tag{8}$$

Finally, the equivalent bump stiffness is $k_B^i$ is given by Eq. (9).

$$k_B^i = \frac{F_p^i}{\Delta\overline{w}^i} = \frac{2\left(\Delta u^i - \Delta u^{i+1}\right) k_s + 0.5\Delta\overline{w}^{i+1}\left(\frac{1}{\tan\alpha^{i+1}} + \mu^{i+1}\right)\left(1 + \chi^{i+1}\tan\alpha^{i+1}\right)}{0.5\Delta\overline{w}^i\left(\frac{1}{\tan\alpha^i} - \mu^i\right)\left(1 - \chi^i\tan\alpha^i\right)} \cos\left(\psi_B\right) \tag{9}$$

Due to the friction forces the movement of each bump segment is iteratively analysed. Starting at the first bump $N_B$ under consideration of three different cases by evaluating the state of Eq. (6): "moving rightward" ($F_f^i < F_x^i$), "moving leftward" ($-F_f^i > F_x^i$) and "stick" ($-F_f^i \geq F_x^i \leq F_f^i$). It is important to note, that the stiffness will significantly increase if both bump segments are in "stick" condition. In this state, the kinematic relationship of Eq. (5) is not valid. A different bump stiffness is calculated by assuming fixed pivots and elastic bump levers, while the stiffness of a lever is named $k_s'$ (see appendix).

$$k_B^i = \frac{F_p^i}{\Delta\overline{w}^i} = \frac{2\left(2R_B \sin\left(\frac{\varphi_B^i}{2}\right) - \Delta u'\right) k_s'}{\Delta\overline{w}^i} \cos\left(\psi_B\right) \tag{10}$$

Where

$$\Delta u' = \sqrt{R_B^2 + \left(R_B - \Delta\overline{w}^i\right)^2 - 2R_B\left(R_B - \Delta\overline{w}^i\right)\cos\left(\varphi_B^i\right)} \tag{11a}$$

$$\cos\left(\psi_B\right) = \frac{\Delta u'^2 + \left(R_B - \Delta\overline{w}^i\right)^2 - R_B^2}{2\Delta u'\left(R_B - \Delta\overline{w}^i\right)} \tag{11b}$$

The damping ability of the compliant structure is considered by applying equivalent viscous dampers, which include the structural loss effects due to Coulomb friction. It is based on the global bump stiffness matrix $[\mathbf{K}_B^*]$ and multiplied term of the loss factor $\gamma$ divided by the excitation frequency $\omega_s$, see Eq.(12).

$$[\mathbf{C}_{eq}^*] = \frac{\gamma}{\omega_s}[\mathbf{K}_B^*] \tag{12}$$

The loss factor is experimentally determined by using static hysteresis curves of a GFB with and without shims. In this work it is set to a value of $\gamma = 0.2$.

### 2.3 Impact of shims on the nominal bearing clearance

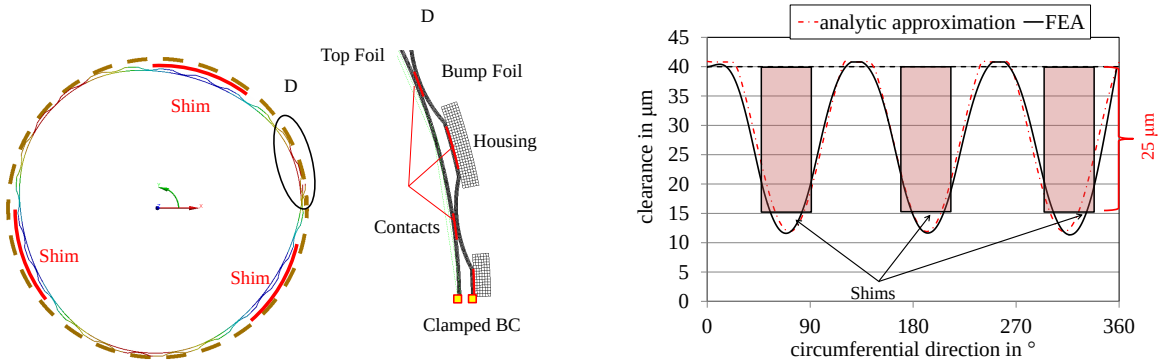


**Figure 4**: Non-linear FEA displacement (40x scaling) and model description (a) bearing clearance along the circumferential direction FEA vs. analytic approximation (b)

Shims affect the nominal bearing clearance $c$ along the circumferential direction ($c\left(\theta\right)$). Hence a non-linear structural FEA has been carried out to analyse the effect of inserting three metal shims (thickness 25 $\mu$m) between the bump-foil and the housing. Note all geometrical data are listed in table 1. In figure 4 a) the deformed elastic structure, modelled as a 2d model under considering the plane stress theory and large displacements is shown. The boundary condition is a fixed-condition for the top- and bump-foil at the welded spot. The contacts are described by an Argument-Lagrange algorithm including frictional behaviour with ($\mu = \chi = 0.1$), while the shims are modelled as an contact displacement interaction (housing/ bump segment) by using 25$\mu$m shim thickness. The difference between the non-shimmed nominal bearing clearance ($c = 40\mu$m) and the radial displacement of the top foil along the circumferential direction is plotted in figure 4 (b) a periodically shaped characteristic, which includes the effects of the welded spot at 0° is shown. Further, a periodically shaped approximation is constructed and shows a good correlation. It is used as the shimmed bearing clearance $c\left(\theta\right)$.

## 3 Validation of the numerical model

In figure 5 (a) and (b) a numerical validation is shown. A bump strip with ten bumps is modelled and different loading cases (decreased (a) and in-/decreased (b)) are applied. The geometrical data are listed in table 1. All loadings are related to an absolute pressure of 2 bar. The link-spring model is validated with FEA results of [25]. Note Le Lez et al. [25] have not considered friction coefficients higher than $\mu = 0.1$. Hence, a additional non-linear FEA by using a commercial code have been performed. The simplified link-spring-model (dashed line) indicates a good correlation with the FEA. However, the results of the bump-spring model generate higher displacements than the FEA and there are differences close to the bump 1 (fixed end). The FEA detected that the bumps push upwards (against the loading direction) while moving leftwards, also find in ref. [1]. The moving direction was detected, but due to the model assumptions no upward moving is possible. The interaction between the fluid film and the

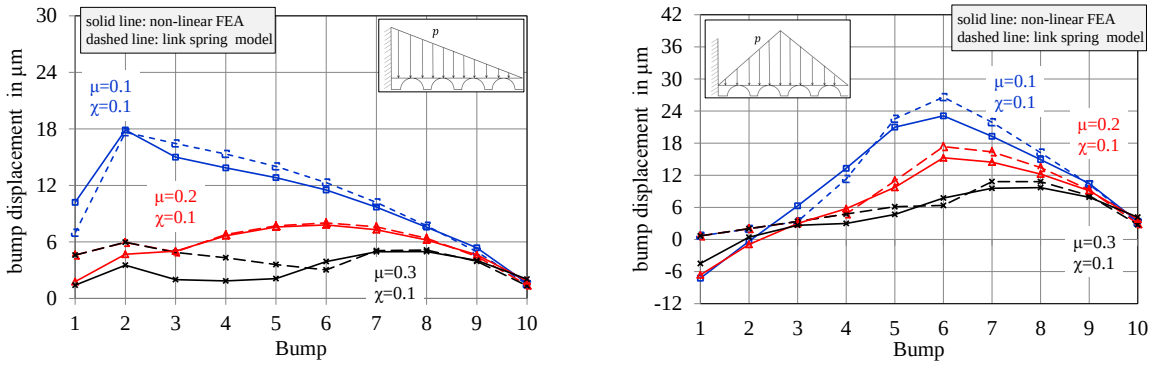


**Figure 5**: Validation of a elastic bump-top foil stripe (10 Bumps) under consideration of different loadings (decreasing (a)) and (increasing (b)) and friction coefficients

structural model is validated by using the experimental data given by [26]. These data are the most detailed open access results. The simulations are based on a set of loadings (5-200 N) at a constant speed of 45 krpm. The authors reported a nominal bearing clearance of 31.8 $\mu m$. However, the nominal bearing clearance is usually estimated by static hysteresis tests and can be affected by uncertainty and measurement failures. Hence, in this work it assumed with 21 $\mu m$ to improve the numerical results, as shown in figure 6 (a). The numerical results indicate a reasonable overall correlation with the experimental data. As shown in the diagram increasing load decreases the minimum film thickness and the film along the edges is smaller compared to the midline. In addition, figure 6 (b) presents the minimum film thickness versus the circumferential direction. Experimental data are compared with the simulated results at the bearing midline. The applied vertical loading and speed conditions are $W = 131.4$ N and $n = 30$ krpm. The results agree very well especially in the zone of smallest film thickness (140-240°). Due to increasing the top foil Young-modulus by a factor of 4 no significant sagging is notable. However, there is still a significant difference between the numerical and experimental results in the low loaded regions ($0 - 140°$ and $240 - 360°$).

## 4 Numerical Results

In this section numerical results of a first generation GFB (case 1) and the same GFB including three metal shims (case 2) are shown. Note the nominal clearance of case 2 is increased to 40 $\mu m$ to add the shims. The geometrical data of the bearing is listed in table 1. The shims (25 $\mu$m) are equally spaced and influence the nominal bearing clearance, as shown in figure 4 (b). In this case study the bearing configurations are varied by three different vertical loadings (5, 15 and 30 N) and rotor speeds up to 80 krpm. The impact of the static and dynamic performance will be analysed.

### 4.1 Static Performance

Figures 7 (a)-(c) present the predicted static load performance of case 1 (first generation GFB) and case 2 (shimmed GFB) vs. the rotor speed. The static equilibrium position is shown in the locus trajectory (figure 7 (a)), increasing the rotor loading results in higher vertical displacements while increasing rotor speed decrees the eccentricities. Interestingly, the trajectories of case 2 are close to the center position ($\varepsilon_x = \varepsilon_y = 0$). Note the magnitude of the eccentricity vs. the rotor speed is plotted in figure 7 (b) and indicates the same trend. Due to the

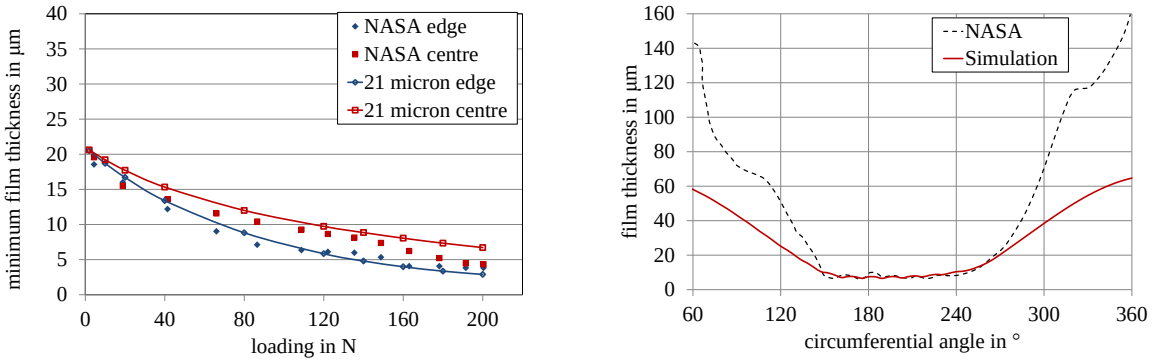


(a) (b)

**Figure 6**: Minimum film thickness vs. rotor loading (45 krpm $c_0 = 21\mu m$) (a) and film thickness along the midline (loading $W = 134.1$ N, 30 krpm) (b). Experimental data [26]

**Table 1**: Geometrical data GFB case 1 and 2

| Parameter | Variable | Value | Unit |
|---|---|---|---|
| bearing radius | $R$ | 19.05 | mm |
| bearing length | $l$ | 38.1 | mm |
| bump thickness | $t_B$ | 0.102 | mm |
| bump pitch | $s_0$ | 4.566 | mm |
| bump arc angle | $\varphi_B$ | 51.5 | ° |
| bump number | $N_\mathrm{B}$ | 26 | - |
| half bump length | $l_0$ | 1.778 | mm |
| clearance case 1 | $c$ | 31.8 | $\mu$m |
| clearance case 2 | $c$ | 40 | $\mu$m |
| foil thickness | $t_F$ | 0.1016 | mm |
| Young-modulus | $E$ | $2.13 \cdot 10^5$ | $\frac{\mathrm{N}}{\mathrm{mm}^2}$ |
| Poison ratio | $\nu$ | 0.29 | - |
| shim thickness | $t_S$ | 25 | $\mu$m |
| shim width | $b_S$ | 12 | mm |

reduced nominal clearances as shown in figure 4 (b) the minimum film thickness is smaller and generates higher peak pressures, which finally stiffens the system. Thus the generated eccentricities and the minimum film thickness are much smaller for case 2 compared to case 1, figure 7 (b)-(c). Higher rotor speeds result in higher load capacities and also drop the eccentricities, which results in thicker gas films. This overall behaviour has an influence on the dimensionless drag torque (t), as shown in figure 7 (c). An increase of rotor speeds and loadings generate higher torque losses. Further, the drag torque of the shimmed configuration (case 2) reduces the losses with increasing the rotor speed due to smaller film thickness.

### 4.2 Dynamic Performance

$$\begin{bmatrix} m_r & 0 \\ 0 & m_r \end{bmatrix} \begin{Bmatrix} \ddot{x} \\ \ddot{y} \end{Bmatrix} + \begin{bmatrix} c_{xx} & c_{xy} \\ c_{yx} & c_{yy} \end{bmatrix} \begin{Bmatrix} \dot{x} \\ \dot{y} \end{Bmatrix} + \begin{bmatrix} k_{xx} & k_{xy} \\ k_{yx} & k_{yy} \end{bmatrix} \begin{Bmatrix} x \\ y \end{Bmatrix} = \begin{Bmatrix} 0 \\ 0 \end{Bmatrix} \tag{13}$$

A simple eigenvalue problem (Eq. 13) is used to evaluate the dynamic performance of the bearing configurations (case 1 and case 2). Linearised bearing parameters (stiffness and damping) (Eq. 14) are calculated to investigate the dynamic performance of a mechanical system supported by a GFB. The eigenvalue problem is calculated by applying Lund's approach [27], which is based on a perturbation method. It delivers the damping and stiffness

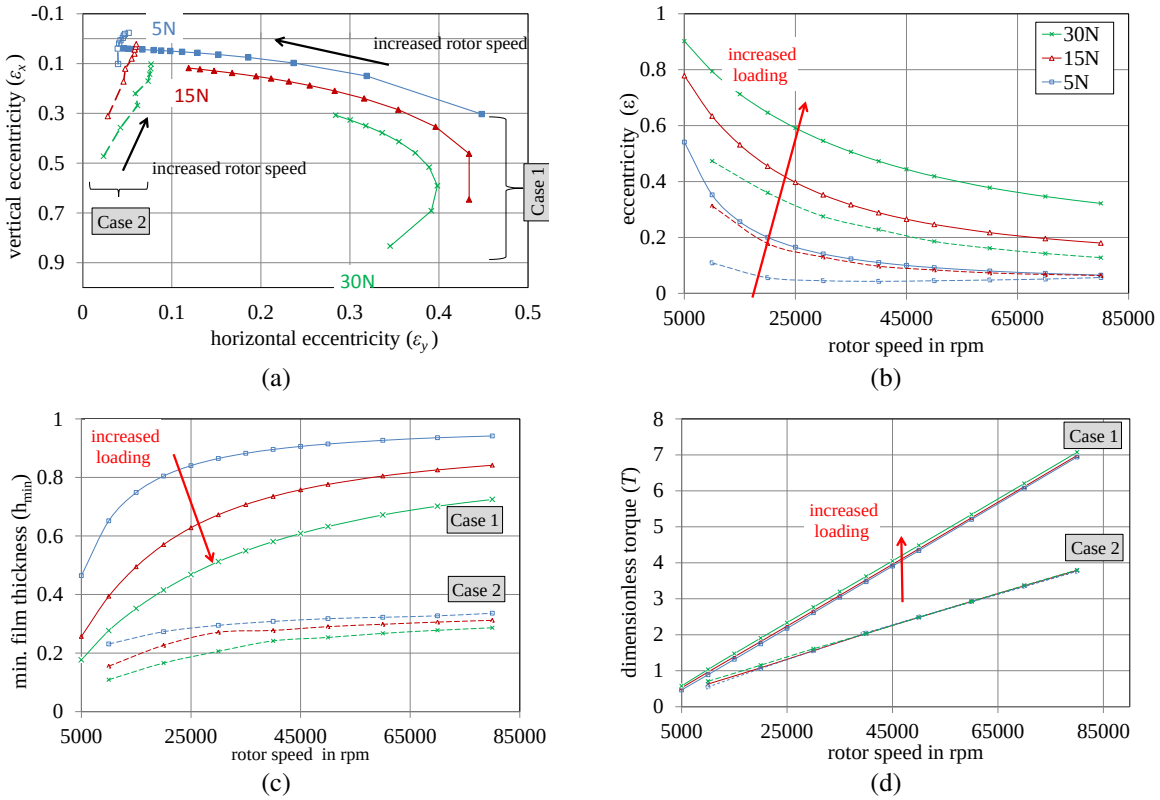


**Figure 7**: Static performance: Trajectory (a), magnitude of eccentricity vs. rotor speed (b), min. film thickness vs. rotor speed (c) and drag torque vs. rotor speed (c). (solid line case 1 and dashed line case 2)

values related to the perturbed pressure field for a single excitation frequency $\omega_s$, ref. [23]. Note the linearised stability results in the onset speed of instability (OSI). Numerical investigations have shown that this speed is well correlated with the onset speed of sub harmonic vibrations (OSSV), ref. [12].

$$[\mathbf{K}] + j\omega_s[\mathbf{C}] = \frac{R^2 p_a}{c} \int_0^{\frac{l}{R}} \int_0^{2\pi} \begin{bmatrix} P_x \cos\theta & P_y \cos\theta \\ P_x \sin\theta & P_y \sin\theta \end{bmatrix} \mathrm{d}Z\mathrm{d}\theta \tag{14}$$

In figure 8 the critical mass parameters vs. the rotor speed are plotted. The curved lines related to a constant loading (isoquant) are calculated by solving the eigenvalue problem. These isoquants indicate the ability of carrying the critical mass with absence of an unstable behaviour and show a convex character, where a higher loading results in higher critical masses. Further, three constant dashed lines are shown. These are based on the constant rotor loadings (5, 15 and 30 N) due to the journal mass ($m_r = W/g$). The intersection between the calculated isoquants (curved lines) and the constant lines finally delivers the onset speed of instability (OSI). The results show that for case 1 an increase of bearing load results in higher OSIs (14.4, 15.9 and 18.43 krpm for 5, 15 and 30 N). However, the OSI is significantly raised for the shimmed GFB (case 2); 65.9, 35.9 and 39.4 krpm for 5, 15 and 30 N, but no clear trend of gaining OSI vs. bearing loading is observed. Thus an optimal shimming needs to be taken into account for each type of bearing configuration, ref. [28]. Nevertheless, the level of the isoquants of case 2 are still higher for increased loadings.

Figure 9 shows the linearised stiffness and damping parameters vs. excitation frequency ratio $\eta = \omega_s/\Omega$ for 5N loading at 10 and 65.9 krpm rotor speed, where the last speed is based on the OSI at 5N loading of case 2. The vertical dashed line for the 65.9 krpm state at $\eta = 0.43$ marks the whirl frequency ratio (WFR) of case 2. In general, increasing the excitation frequency ratio results in stiffer gas films in the direct direction while cross-coupling effects are reduced, same effects are also present for an increasing of rotor speeds, see figure 9 (a) and (b). In figure 9 (c) and (d) the direct damping are decreased in the lower sub harmonic excitation ratio range, but raise for higher excitation frequency ratios and finally drop for super harmonic excitation.

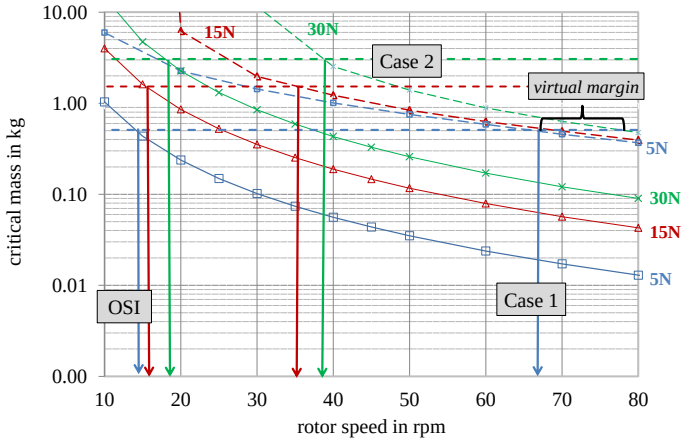


**Figure 8**: Bearing parameters vs. excitation frequency ratio (Case 2 dashed and Case 1 solid line)

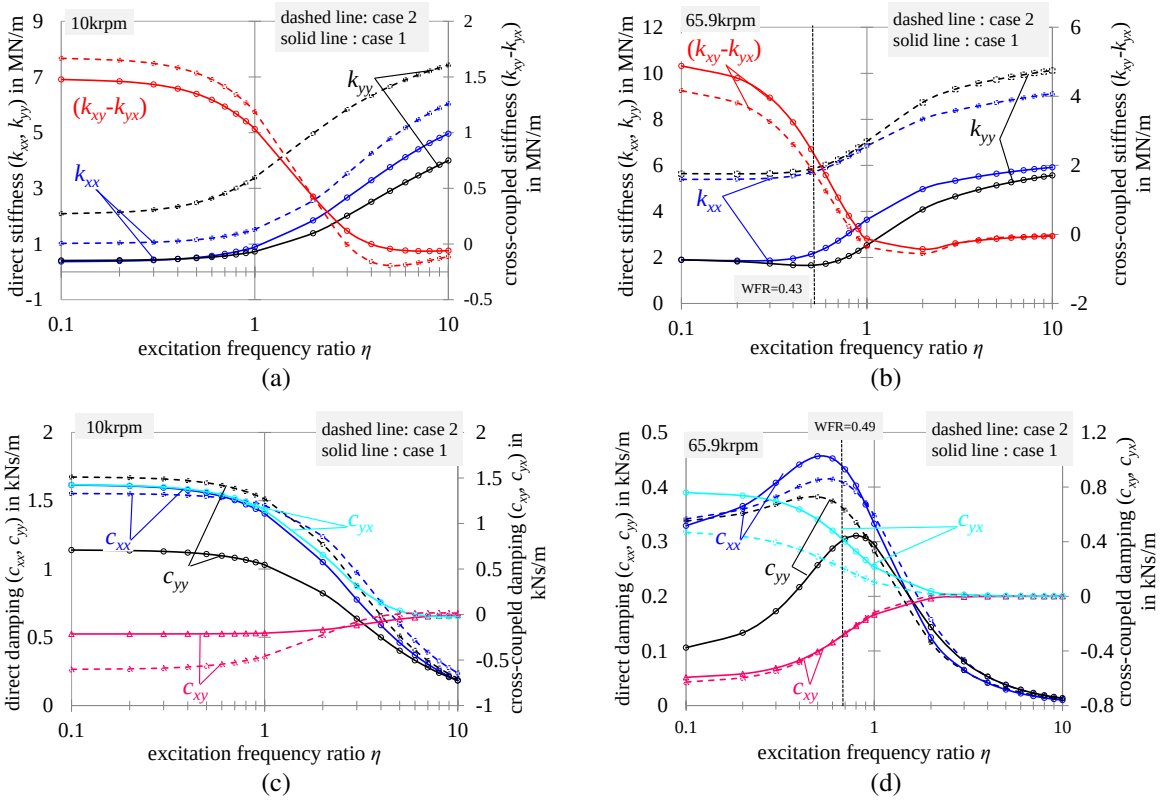


**Figure 9**: Bearing parameters stiffness (a)(b) and damping (c)(d) vs. excitation frequency ratio (Case 1 dash and Case 2 solid line), $W$=5 N, n=10 and 65.9 krpm.

As shown in the figure 9 (a) the stiffness of the direct direction is much smaller for case 1 compared to case 2. For case 2, the vertical stiffness ($k_{xx}$) is increased compared to the horizontal stiffness ($k_{yy}$) (*orthotropic effect*), while a converse behaviour is shown for the case 1. Further, case 2 has slightly increased cross-coupling stiffness effects ($k_{xy} - k_{yx}$) compared to case 1. Note the cross-coupling effects have a major influence on the linearised stability, ref. [23]. However, due to increased direct stiffness *orthotropic effects* and higher direct damping for case 2 at speeds of 10 up to 65.9 krpm, a higher OSI is obtained and the destabilising effect of the cross-coupling stiffness is compensated over the speed range. Further, at the OSI (65.9 krpm, case 2) the *orthotropic effect* is not so significant. This finally results a shift of the isoquant towards higher OSIs, as shown in figure 8. In figure 10 the linearised bearing parameters are plotted for case 2 at 65.9 krpm (OSI 5N case 2). Comparing the 5N with the 30N loading

condition illustrates, that higher loadings decrease the cross-coupling stiffness effects slightly. However, the overall stiffness and damping behaviour at the excitation frequency of 0.43, which is related to the critical whirl frequency ratio (WFR) indicates similar parameters. This similarity finally results in small inclinations of the isoquants of the critical mass parameter towards higher rotor speeds, which is indicated by the virtual margin. It can also be explained by the physical effect of *gas hardening*, which stiffens the gas film at high rotor speeds. The stiffness and damping characteristic is finally influenced by the elastic non-linear structure and its modifications. Thus, gaining of OSI is achieved by reducing the constant rotor mass, see figure 8.

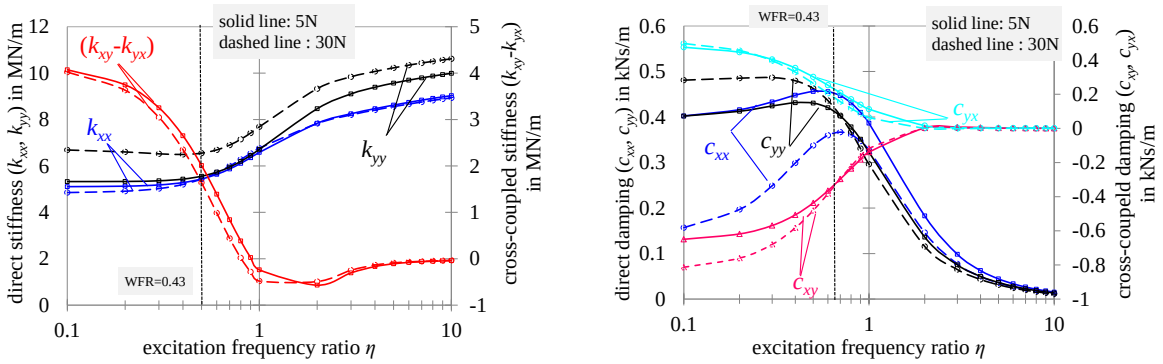


**Figure 10**: Bearing parameters stiffness (a) and damping (b) vs. excitation frequency ratio (5N solid and 30N dash line), Case 2, n=65.9 krpm.

## 5 Conclusions

This paper has firstly used a non-linear model which includes frictional contacts inside the elastic structure and bump interactions. It has been validated with a numerical non-linear FEA analysis and experimental data supplied by open literature [26] and has shown good correlation. A non-linear FEA has been applied to identify the influence of shimming on the nominal bearing clearance. Further, a numerical case study of a first generation GFB and a shimmed GFB has been carried out. The results of this paper show that:

1. Shims decrease the drag torque, resulting in smaller film thickness and closer centre position operation.
2. Shims stiff the bearing system significantly, while cross coupling effects for the low loaded state (5N) have been slightly increased.
3. Shims have increased the OSSV for the considered vertical loadings with gains of (5N; 357%), (15N; 126 %) and (30N; 114%) related to a GFB without shims. The main cause of this behaviour is the increased orthotropic direct stiffness.

As shown in the results an optimal shimming may improve dynamic performance. Hence, future work will consider different shim patterns. Furthermore, the shim model will be extended to a dynamic structural model. It will be validated with experimental data. Therefore experiments of a shimmed GFB will be performed to analyse the structural behaviour in static and dynamic load tests. And a test rig for parameter identification will be used to examine the theoretical findings.

## REFERENCES


[1] Feng, K., and Kaneko, S., 2010. “Analytical model of bump-type foil bearings using a link-spring structure and a finite-element shell modell”. *ASME J. Tribol.,* **132**(1), S. 021706–1– 021706–11.

[2] DellaCorte, C., and Valco, M., 2000. “Load capacity estimation of foil air journal bearings for oil-free turbomachinery applications”. *STLE Tribol. Trans.,* **43**, S. 795–801.

[3] Heshmat, H., 1994. “Advancements in the performance of aerodynamic foil journal bearings: High speed and load capability”. *ASME J. Tribol.,* **116**(2), S. 287–294.

[4] Ku, C.-P., and Heshmat, H., 1994. “Structural stiffness and coulomb damping in compliant foil journal bearings: Parametric studies”. *STLE Tribol. Trans.,* **37**(3), S. 455–462.

[5] Rubio, D., and San Andrés, L., 2007. "Structural stiffness, dry friction coefficient, and equivalent viscous damping in a bump-type foil gas bearing". *ASME J. Eng. Gas Turbines Power,* **129**(2), S. 494–502.

[6] Larsen, S. J., Varela, A. C., and Santos, I. F., 2014. "Numerical and experimental investigation of bump foil mechanical behaviour". *Tribol. Int.,* **74**, S. 46 – 56.

[7] Heshmat, H., 2000. "Operation of foil bearings beyond the bending critical mode". *ASME J. Tribol.,* **122**(2), S. 478–479.

[8] Kim, K.-S., Cho, B.-C., and Kim, M.-H., 2010. Rotordynamic characteristics of 65kw micro turbine with compliant air foil bearings. Proceedings: IFToMM 2010 - 8th International Conference on Rotor Dynamics, Seoul, Korea.

[9] Kim, T. H., 2007. "Analysis of side end pressurized bump type gas foil bearings: A model anchored to test data". Dissertation, Texas A&M University, College Station.

[10] Sim, K., Lee, Y.-B., Kim, T. H., and Lee, J., 2012. "Rotordynamic performance of shimmed gas foil bearings for oil-free turbochargers". *ASME J. Tribol.,* **134**(3), S. 031102–1–031102–11.

[11] San Andrés, L., Rubio, D., and Kim, T. H., 2007. "Rotordynamic performance of a rotor supported on bump type foil gas bearings: Experiments and predictions". *ASME J. Eng. Gas Turbines Power,* **129**(3), S. 850–857.

[12] Hoffmann, R., Pronobis, T., and Liebich, R., 2014. Non-linear stability analysis of a modified gas foil bearing structure. Proceedings: IFToMM 2010 - 9th International Conference on Rotor Dynamics, Milano, Italy.

[13] San Andrés, L., and Kim, T., 2008. "Forced nonlinear response of gas foil bearing supported rotors". *Tribol. Int.,* **41**(8), S. 704 – 715.

[14] Heshmat H., Chen H. M., W. J. F., 2000. On the performance of hybrid foil-magnetic bearings. J. Eng. Gas Turbines Power 2000;122:73-81.

[15] Heshmat, H., Shapiro, W., and Gray, S., 1982. "Development of foil journal bearings for high load capacity and high speed whirl stability". *ASME J. Lubr. Technol.,* **104**(2), S. 149–156.

[16] Kim, T. H., and San Andrés, L., 2009. "Effect of side feed pressurization on the dynamic performance of gas foil bearings: A model anchored to test data". *ASME J. Eng. Gas Turbines Power,* **131**(1), S. 012501.

[17] Hoffmann, R., Pronobis, T., and Liebich, R., 2014. Stability analysis of a pressurized gas foil bearings for high speed applications. Proceedings: 11th International Conference of Turbocharging, London.

[18] Kim, D., and Varrey, M. K., 2012. "Imbalance response and stability characteristics of a rotor supported by hybrid air foil bearings". *STLE Tribol. Trans.,* **55**(4), S. 529–538.

[19] Kim, D., and Lee, D., 2010. "Design of three-pad hybrid air foil bearing and experimental investigation on static performance at zero running speed". *ASME J. Eng. Gas Turbines Power,* **132**(12), S. 122504–1–122504–10.

[20] Ku, C.-P. R., 1994. "Dynamic structural properties of compliant foil thrust bearings-comparison between experimental and theoretical results". *ASME J. Tribol.,* **116**(1), S. 70–75.

[21] Lee, Y. B., Kim, T. H., Kim, C. H., Lee, N. S., and Choi, D. H., 2004. "Dynamic characteristics of a flexible rotor system supported by a viscoelastic foil bearing (vefb)". *Tribol. Int.,* **37**, S. 679–687.

[22] Heshmat, H., 1991. "Analysis of compliant foil bearings with spatially variable stiffness". In Proceedings: AIAA, SAE, ASME, and ASEE, Joint Propulsion Conference, 27 th, Sacramento, CA.

[23] Hoffmann, R., Pronobis, T., and Liebich, R., 2014. The impact of modified corrugated bump structures on the rotor dynamic performance of gas foil bearings. Proceedings: ASME GT2014-25636, DÃ $\frac{1}{4}$sseldorf.

[24] San Andrés, L., and Kim, T., 2007. "Improvements to the analysis of gas foil bearings: Integration of top foil 1d and 2d structural models". *Proceedings: ASME Paper No. GT2007-27249*.

[25] Le Lez, S., Arghir, M., and Frene, J., 2007. "A new bump-type foil bearing structure analytical model". *ASME J. Eng. Gas Turbines Power,* **29**(129), S. 1047–1057.

[26] Ruscitto, D., Mc Cormick, J., and Gray, S., 1978. Hydrodynamic air lubricated compliant surface bearing for an automotive gas turbine engine i - journal bearing performance. Technical Report NASA CR-135368.

[27] Lund, J. W., 1968. "Calculation of stiffness and damping properties of gas bearings". *ASME J. Lubr. Technol.,* **90**(4), S. 793–803.

[28] Schiffmann, J., and Spakovszky, Z. S., 2013. "Foil bearing design guidelines for improved stability". *ASME J. Tribol.,* **135**, S. 011103–1– 011103–11.

## Nomenclature

| | | | |
|---|---|---|---|
| $[\mathbf{C}]$ | GFB damping matrix | $c$ | bearing nominal radial clearance |
| $E$ | Young-modulus | $g$ | gravitational constant |
| $\{\mathbf{f}_B\}$ | reaction force vector | $f_e$ | eigenfrequency |
| $h$ | film thickness | $h_{n,m}$ | impedance $(n,m)=(x,y)$ |
| $h_B$ | bump height | $j$ | complex number $j=\sqrt{-1}$ |
| $K_f$ | bump stiffness factor | $[\mathbf{K}^*]$ | global stiffness matrix GFB structure |
| $[\mathbf{K}]$ | GFB stiffness matrix | $l$ | bearing axial length |
| $l_0$ | half bump length | $m_r$ | journal mass |
| $N_B$ | number of bumps | $p$ | pressure |
| $R$ | bearing radius | $t$ | time |
| $t_B$ | bump foil thickness | $t_F$ | top foil thickness |
| $s_0$ | bump pitch | $x,y,z$ | inertial coordinate system |
| $\beta$ | attitude angle | $\varepsilon$ | eccentricities |
| $\mu$ | dynamic viscosity | $\eta$ | excitation frequency ratio |
| $\gamma$ | structural loss factor | $\nu$ | Poisson's ratio |
| $\varphi_B$ | Bump pitch angle | $\mu,\chi$ | friction coefficient |
| $\Lambda$ | eigenvalue | $\omega_s$ | excitation frequency ($\omega_s=2\pi f_s$) |
| $\Omega$ | rotor angular speed | $\theta$ | circumferential coordinate |

## Abbreviations

| | |
|---|---|
| **GFB** | Gas Foil Bearing |
| **WFR** | Whirl Frequency Ratio $WFR=\frac{\omega_i}{\Omega}$ |
| **OSI** | Onset Speed of Instability |
| **OSSV** | Onset Speed of Subsynchronous Vibration |

## Appendix

Structural interaction forces are based on the deformed springs ($k_s$ "moving" and $k_s'$ "stick" condition). These springs are calculated by using Castigliano's theorem, ref. [1, 25]

$$k_s=\left\{\frac{R_B^2}{2lS}\left[2\varphi_B^i-4\frac{\sin^2\left(\varphi_B^i\right)}{\varphi_B^i}+\sin\left(2\varphi_B^i\right)\right]+\frac{R_B}{t_b l E_B}\left[\varphi_B^i+\frac{\sin\left(2\varphi_B^i\right)}{2}\right]\right\}^{-1} \tag{15a}$$

$$k_s'=\left\{\frac{R_B}{2lS}\left[2f_1\left(\frac{\varphi_B^i}{2}+f_2\left(\varphi_B^i\right)\cdot f_3\left(\varphi_B^i\right)\right)+\frac{R_B}{2E_B t_B l}\left(2f_4\left(\frac{\varphi_B^i}{2}\right)\right)\right]\right\}^{-1} \tag{15b}$$

where $S=E_B t_b^2/(12\left(1-\nu^2\right))$ and the terms $f_1$, $f_2$, $f_3$ and $f_4$ are functions of the bump geometry, ref. [1].